J Catal. 2020 Sep; 389: 1–8.
PMCID: PMC7539370
doi: 10.1016/j.jcat.2020.04.009: 10.1016/j.jcat.2020.04.009

Enhanced chlorine evolution from dimensionally stable anode by heterojunction with Ti and Bi based mixed metal oxide layers prepared from nanoparticle slurry

Sukhwa Hong,[a] Tai-kyu Lee,[b] Michael R. Hoffmann,[c] and Kangwoo Cho[a,d,*]

[a]Division of Environmental Science and Engineering, Pohang University of Science and Technology (POSTECH), Pohang 790-784, Republic of Korea
[b]Nanopac Co., Ltd. 673 Hwasan-Ri, Cheoin-Gu, Yongin-Si, Gyeonggi-Do, Republic of Korea
[c]Linde+Robinson Laboratories, California Institute of Technology, 1200 E. California Blvd., Pasadena, CA 91125, USA
[d]Institute for Convergence Research and Education in Advanced Technology (I-CREATE), Yonsei University International Campus, Incheon, Republic of Korea
Kangwoo Cho: kwcho1982@postech.ac.kr
*Corresponding author. kwcho1982@postech.ac.kr

Received 2019 Dec 22; Revised 2020 Mar 4; Accepted 2020 Apr 10.

Graphical abstract

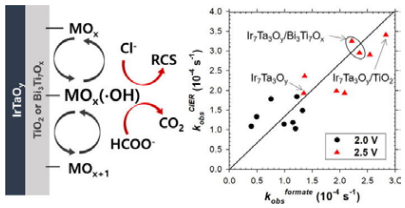

Keywords: Heterojunction anode, Reactive chlorine species, Wastewater treatment, Dimensionally stable anode, TiO_2

Abstract

This study reports enhanced current (CE_{RCS}) and energy efficiency (EE_{RCS}) of reactive chlorine species

(RCS) generation on $Ir_7Ta_3O_y$ anode by Ti/Bi mixed metal oxide heterojunction layers despite reductions in pseudo-capacitance and film conductivity. In potentiostatic electrolysis of 50 mM NaCl solutions, dramatic improvement (0.61 mmol cm^{-2} hr^{-1} at 2.5 V NHE) was noted by simple coating of thin (~2 μm) TiO_2 layer from ball-milled TiO_2 nanoparticle (80–100 nm) suspension, even with moderate elevation in voltammetric wave. Decoration of Bi_2O_3 particles (1 – 2 μm) showed limited or adverse effects for RCS generation and stability. However, Bi-doped TiO_2 layers prepared from polyol-mediated or co-precipitation methods marked the highest CE_{RCS} (~100%) and EE_{RCS} (8.16 mmol Wh^{-1} at 2.5 V NHE) by increased mixing level and effective shift in surface charge. Surface ·OH exclusively mediated the RCS generation whose further transformation to higher oxide could be restrained by the heterojunction layer.

1. Introduction

Chlorine (Cl_2) is a widely utilized industrial reagent for polymer synthesis globally. In chemical industry, chlor-alkali process would be one of the most commercialized methods to electrolyze concentrated NaCl solutions for generation of Cl_2, H_2, and caustic soda (NaOH). Dimensionally stable anodes (DSAs), based on precious metal oxides such as RuO_2 and IrO_2, have been most often used for these purposes owing to the supreme activity and stability [1], [2], [3]. Variable secondary components have been explored primarily for stability enhancement, to come up with the mixed metal oxide anodes, $Ir_7Ta_3O_x$ and $Ru_3Ti_7O_x$ as the optimal DSAs compositions for many decades [1], [3], [4].

Aqueous Cl_2 (commonly noted as free chlorine) is also a famous oxidant for drinking water disinfection and, recently, electrolytic reactive chlorine species (RCS) has been utilized for on-site treatment of saline wastewater as well [5]. Owing to the value consuming nature of environmental technologies, however, the scarcity of Ir and Ru components have substantially constrained a large scale application of the electrochemical chlorination for water treatment. In addition, the DSAs active for chlorine evolution reaction (ClER, $E°(Cl_2/Cl^-)$ = 1.36 V NHE) also effectively catalyze oxygen evolution reaction (OER, $E°(O_2/H_2O)$ = 1.23 V NHE) [6], a parasitic side reaction with respect to the water treatment. A sufficient anodic potential bias on hydrous metal oxide (>MO_x) would initiate the formation of surface hydroxyl radical (>MO_x(·OH), Eq. (1)) whose further oxidation could lead to higher oxide (>MO_{x+1}, *via* Eq. (2)) formation. It has been widely accepted that the overall adsorption energy of oxygen to metal (M−O bond strength) is known to be the principal factor of OER activity mostly *via* Eq. (4) [7], [8], [9], [10].

$$> MO_x + H_2O \rightarrow > MO_x(\cdot OH) + H^+ + e^- \quad (1)$$

$$> MO_x(\cdot OH) \rightarrow > MO_{x+1} + H^+ + e^- \quad (2)$$

$$> MO_x(\cdot OH) \rightarrow > MO_x + 1/2\ O_2 + H^+ + e^- \quad (3)$$

$$> MO_{x+1} \rightarrow > MO_x + 1/2\ O_2 \quad (4)$$

In a presence of chloride ions, parallel ClER mechanism on metal oxide electrocatalysts can be described by Eqs. (5), (6), where the ClER could share active sites with the competing OER [6], [8]; *i.e.*, MO_x(·OH) and MO_{x+1} mediate the ClER as well.

$$> MO_x(\cdot OH) + Cl^- \rightarrow > MO_x + 1/2\ Cl_2 + OH^- \quad (5)$$

$$> MO_{x+1} + Cl^- \rightarrow > MO_x + ClO^- \quad (6)$$

Therefore, the selectivity towards ClER should be an important consideration for an energy-efficient electrochemical RCS mediated water treatment, especially considering limited Cl^- concentration (<50 mM) in (waste)water electrolyte [11].

Specific group of metal oxides such as PbO_2, SnO_2, and TiO_2 could be characterized by a weak bond strength between metal and active oxygen to predominantly exist in the >MO(·OH) form which would prefer ClER due to stronger oxidation power than MO_{x+1}. In particular, TiO_2 is non-toxic and widely-used earth-abundant catalysts to provide > Ti(·OH) under an anodic potential with high surface density. Nevertheless, relatively large kinetic barrier for the water discharge has limited the utilization of TiO_2 as an electrocatalyst. We previously proposed a heterojunction architecture with coating TiO_2 layers with or without mixing Bi ($Bi_xTi_{1-x}O_z$) on top of $Ir_7Ta_3O_y$ DSA for an enhanced RCS generation in dilute aqueous solutions [11]. In these configurations, conductor-like nature of $IrTaO_y$ could serve as an ohmic contact to Ti substrate [11], [12], while surface hydrous TiO_2 (>Ti(OH^-)) provided elevated quasi-stationary concentration of >MO_x(·OH). In spite of limited consideration for limited active sites and different kinetic parameters to predict selectivity in parallel reactions, density functional theory (DFT) calculations on model RuO_2/TiO_2 architecture [13] further suggested that the TiO_2 heterojunction layer could shift locations in volcano plots of OER and ClER, which in-turn influences the ClER selectivity. In addition, mixing Bi in the outer layer was evinced to increase electrostatic sorption of anions (Cl^-). In our earlier contribution, nevertheless, the peroxo-route for aqueous Ti-glycolate complex and solution casting of the $Bi_xTi_{1-x}O_z$ layer were rather dangerous and labor consuming.

This study reports simplified preparation methods for coating TiO_2 based heterojunction layers (on $Ir_7Ta_3O_y$ DSA) which was either decorated by Bi_2O_3 micro-particles or mixed with Bi^{3+}. In particular, employing nanoparticle slurry precursors was expected not only to augment the catalytic edge sites [3], but also to allow an effective passivation owing to greater viscosity than aqueous precursor [14]. In dilute (50 mM) NaCl solutions, the activity and selectivity for ClER were comparatively evaluated for the heterojunction anodes with variable outer layer loading (thickness) and mixing levels of Bi. In addition, the roles of >MO_x(·OH) and >MO_{x+1} on the RCS generation were interrogated by correlation with formate ion degradation.

2. Experimental section

2.1. Preparation and characterization of the anodes

All chemical reagents were analytical grade and obtained from Sigma-Aldrich or Daejung chemicals to be used without further purification. Solutions were prepared with Millipore-Q water (Millipore) with a specific resistivity of 18 MΩ cm^{-1}. For pretreatment of the anode base, Ti foils (99.5% Alfa-Aesar) were cleaned with SiC paper, sonicated in organic solvent solutions (equivolumic deionized water, ethanol, and acetone) for 0.5 h, and immersed in 10 wt% oxalic acid for 50 min at 80 °C. The $IrTaO_y$ layer was prepared by soaking the Ti substrate (3 × 2 cm^2, distance = 5 mm) into solutions with 73 mM H_2IrCl_6, and 27 mM $TaCl_5$. 4 N HCl and equivolumic ethanol/isopropanol solutions were compared as solvents. The loaded precursor was sequentially dried at 80 °C and annealed at 525 °C for 10 min, which was repeated five times

before final annealing at 525 °C for 1 h. For preparation of outer heterojunction layers, three different types of precursor were prepared as follows. A) P90 TiO_2 (Evonik Industries) and Bi_2O_3 particles separately ball-milled (Ultra Apex mill) in ethanol to have particle size range of 80–100 nm and 1–2 μm, respectively. The TiO_2 nanoparticles (3.8 wt%) were dispersed in ethanol/terpineol (16:19 wt%) solution with added ethyl cellulose binder (2.2 wt%). Bi_2O_3 micro-particles were added with variable Bi to Ti ratios (0:10, 1:9, and 3:7). B) 6 mL titanium butoxide was added to 150 mL ethylene glycol to be stirred for 8 h in room temperature. The mixture was poured into 510 mL acetone and 8 mL of deionized (DI) water was added before vigorous stirring for 1 h. Resulting precipitate was collected using a centrifuge (6000 rpm for 4 min), washed with ethanol 5 times, and re-dispersed in ethanol with a given concentration of bismuth citrate. C) titanium tetraisopropoxide (1.25 mL) in ethanol (25 mL) was added to 8 mM $Bi(NO_3)_3$ solution (pH 1.5 adjusted by acetic acid) by dropwise and the mixture was stirred overnight. Resulting precipitate was collected (11000 rpm for 10 min), washed with DI water 5 times, and re-dispersed in DI water. These precursors were sprayed on the $IrTaO_y$ layer and annealed at 450 °C for 30 min and the coating procedure was performed for 3 times. In this study, heterojunction anodes from precursor A were denoted as $(Bi_2O_3)_x(TiO_2)_{1-x}$ (x = 0, 0.1, and 0.3), while the outer layers with low mass loading (L) were prepared without repetition to compare the performance with analogues with high mass loading (H). The anodes from precursor B and C with nominal Bi to Ti ratio of 3:7 were named as $Bi_3Ti_7O_x$-1 and $Bi_3Ti_7O_x$-2, respectively, to describe greater mixing level of Bi.

The surface morphologies were observed by using a ZEISS 1550VP field emission scanning electron microscope (SEM) and elemental compositions were estimated using an Oxford X-Max SDD X-ray energy-dispersive spectrometer (EDS) system. The EDS analysis was performed either in a point-and-identification mode for 10 arbitrary sites or in mapping mode. The surface crystallography was assessed by X-ray diffraction (XRD) using an X'pert MD (Panalytical) diffractometer with Cu−K radiation.

2.2. Electroanalysis.

The electrochemical activities of $(Bi_2O_3)_x(TiO_2)_{1-x}$ and $Bi_3Ti_7O_x$-1/2 heterojunction anodes were assessed using linear sweep voltammetry (LSV) and cyclic voltammetry (CV). In a single compartment cell (working volume = 60 mL), each anode was parallel matched with AISI 304 stainless steel cathode (distance = 5 mm) with active geometric surface area of 3 × 2 cm^2. Ag/AgCl/sat. KCl reference electrode (BASI Inc.) was located 3 mm away from the anode center. The three electrodes configuration was connected to a potentiostat (SP-50, Bio-Logic) to control anodic potential (E_a) in normal hydrogen electrode (NHE) scale (E_a (NHE) = E_a (Ag/AgCl) + 0.197 V). The CV and LSV data were recorded with E_a ranges of 0.2–1.0 V NHE (scan rate of 20 mV s^{-1}) and of 0.8–2.0 V NHE (scan rate of 5 mV s^{-1}), respectively. Before all electrochemical experiments, open circuit potentials were measured for 30 min and ohmic resistances were measured by current interruption method at 200 mA current bias.

2.3. Potentiostatic Electrolysis.

The efficiency of RCS generation was evaluated during potentiostatic electrolysis of 50 mM NaCl solutions at variable E_a values (2.0, 2.5, and 3.0 V NHE). The evolution of [RCS] was measured by DPD (N, N-diethyl-p-phenylenediamine) reagents 3 times at 2 min intervals and, during this period, further oxidation of RCS to ClO_3^- or ClO_4^- could be negligible [15]. The specific rate (SR), current (CE) and energy efficiency (EE) of the RCS generation were estimated by the following equations (Eqs. (7)–(9)).

$$SR_{RCS}\ (mmol\ cm^{-2}) = \frac{Vd[Cl_{DPD}]}{Adt} \quad (7)$$

$$CE_{RCS}\ (\%) = \frac{2VFd[Cl_{DPD}]}{Idt} \quad (8)$$

$$EE_{RCS}\ (mmol\ Wh^{-1}) = \frac{Vd[Cl_{DPD}]}{EIdt} \quad (9)$$

where V is electrolyte volume (0.06 L), F is Faraday constant (96485.3 C mol^{-1}), $[Cl_{DPD}]$ is the concentration of RCS (M), t is electrolysis time (s), A is electrode surface area (cm^2), E is cell voltage (V) and I is current (A).

In order to assess the roles of $>MO_x(\cdot OH)$ on RCS generation, formate ion was employed as the ·OH probe compound. The potentiostatic electrolysis of 50 mM NaCOOH solutions was performed for 2 h at E_a 2.0 or 2.5 V NHE. The $[HCOO^-]$ of samples were periodically quantified by ion chromatography (IC, Dionex, USA) with an anion-exchange column (Ionpac AS 19).

3. Results and discussion

3.1. Physico-chemical characteristics of $(Bi_2O_3)_x(TiO_2)_{1-x}$ heterojunction layers

For the heterojunction electrodes, the underlying $IrTaO_y$ layer was synthesized using an organic solvent (ethanol/isopropanol solutions), due to more uniform surface coverage and moderately greater electrochemically active surface area (ECSA) than analogous from hydrochloric acid solvents (Figure S1 and S2). SEM images in Figure S3 show the horizontal surface morphology of the $(Bi_2O_3)_x(TiO_2)_{1-x}$ heterojunction anodes with variable molar ratios of Ti to Bi and catalysts loading (thickness). Cross-sectional SEM images estimated the average thickness of (TiO_2)-L and (TiO_2)-H to be *ca.* 2 and 5 μm, respectively. (TiO_2)-H and -L showed marginal numbers of crack and pinhole that are typically observed for thermally decomposed (mixed) metal oxide electrodes. Since P60 TiO_2 nanoparticles already underwent annealing, further thermal expansion of the crystalline TiO_2 particles could be limited, while the aggregation of nanoparticles would alleviate the topological distortion. For samples with added Bi_2O_3 particles in precursor solutions, discrete islands of bismuth oxide scattered on the surface were noted. EDS mapping in Figure S3g-h clearly identified the immobilized particles (diameter ~ 1 μm) to be Bi_2O_3.

In the absence of Bi mixing ((TiO_2)-L and -H), the primary XRD peaks in Fig. 1 (individual patterns in Figure S4) commonly involved standard patterns of anatase TiO_2 (2θ = 25.2, 37.7, and 47.9°) and less prominently of rutile TiO_2 (2θ = 27.5, 36.1, and 54.4°), being in compatible with the composition of precursory TiO_2 particles (92:8 wt% of anatase:rutile for P60). A phase transition during the thermal annealing at 450 °C would be limited since transformation into the rutile structure is known to occur at a temperature normally exceeding 600 °C [16]. Negligible characteristic pattern of IrO_2 (2θ = 34.7, 40, 54,

and 69.3°) on surface of these anodes indicated relatively thorough covering even with single spray coating. In comparison, $(Bi_2O_3)_3(TiO_2)_7$–L electrodes showed clear patterns of standard α-Bi_2O_3 (2θ = 27.5, 33.2, and 46.5°), while the repeated coating of the Bi/Ti mixed precursor (-H) alleviated the signal from Bi_2O_3 buried in TiO_2 matrix. The addition of Bi_2O_3 particles to the precursor gave negligible changes in diffraction peak positions of TiO_2, indicating limited thermal diffusion between the separate crystalline lattice structures (TiO_2 and Bi_2O_3) [17]. Therefore, each metal oxide phase was expected to maintain the intrinsic physicochemical properties with minimal doping effects; thus, the outer heterojunction layers could be denoted as $(Bi_2O_3)_x(TiO_2)_{1-x}$. In the presence of Bi_2O_3 particles, signals from underlying IrO_2 (peak near 35°) and Ti substrate (peak near 40°) were invigorated. Considering that the XRD analysis was performed after the electrochemical analyses described hereinafter, these observations suggest the instability of bismuth oxide in anodic environment (*vide-infra*).

3.2. Voltammetric responses of $IrTaO_y/(Bi_2O_3)_x(TiO_2)_{1-x}$ heterojunction anodes

Areal capacitance from CV within the potential window of water splitting has often been utilized to estimate the ECSA [18], [19]. Fig. 2a (raw CV data in Figure S5) illustrates the areal capacitance measured under anodic potential between 0.2 and 1.0 V NHE in 50 mM NaCl solutions (circum-neutral pH). The highest areal capacitance (22 mF cm^{-2}) of $IrTaO_y$ was reduced by about 30% upon addition of surface TiO_2 layers. Mixing Bi_2O_3 particles on surface insignificantly affected or even further decreased the areal capacitance. Within the potential scan range, oxidative transformations of hydrous > TiOH or > BiOH (*e.g.*, to oxyhydroxide or higher oxide) could be limited to especially due to the fully oxidized Ti^{4+}. Nevertheless, considering rather thorough surface passivation by TiO_2 layers (at least for $IrTaO_y/TiO_2$ anodes as shown in Fig. 1), the electrochemical activity for the heterojunction anodes would be ascribed to a thermal diffusion of Ir components into the upper layer (*vide infra*) [11].

Linear sweep voltammetry (scan range: 0.8 - 2.0 V NHE, scan rate: 5 mV s^{-1}) in 50 mM NaCl solutions (Fig. 2b) estimated the anodic potential at 10 mA cm^{-2} in the order of TiO_2-L < $IrTaO_y$ < TiO_2-H ~ $(Bi_2O_3)_1(TiO_2)_9$-L ~ $(Bi_2O_3)_3(TiO_2)_7$-L < $(Bi_2O_3)_1(TiO_2)_9$-H ~ $(Bi_2O_3)_3(TiO_2)_7$-H (Table 1). In these experimental conditions, the current generation would be ascribed to parallel OER and ClER. Electrical conductivity of semiconductor electrocatalysts should be another consideration especially for thick catalyst film. To this end, the outer heterojunction layer mostly lowered the current generation due to the inherently poor electrical conductivity of TiO_2 and Bi_2O_3. More pronounced current decline with included Bi_2O_3 particles, particularly with higher loading ($(Bi_2O_3)_1(TiO_2)_9$-H and $(Bi_2O_3)_3(TiO_2)_7$-H), agreed with the concurrent increase in ohmic resistance measured by a current interruption method. The current interruption would collectively evaluate the electrolyte resistance of ion migration, polarization resistance and resistance across the catalytic film, often described as resistances in series in an equivalent circuit [20]. Since the Bi_2O_3 particles were speculated to be anchored within TiO_2 matrix without a direct contact with $IrTaO_y$ layer, $(Bi_2O_3)_x(TiO_2)_{1-x}$ anodes would suffer from invigorated resistance across the multiple junctions ($IrTaO_y/TiO_2/Bi_2O_3$).

Nevertheless, the observed OER and ClER activities were incompletely justified with the areal capacitance and ohmic resistance, particularly for the unexpected elevated current generation from TiO_2-L anode. A recent report presented evidences that the OER and ClER overpotential values of IrO_2 could be reduced upon a few cycles of atomic layer deposition (ALD) of thin TiO_2 layer by shifting surface charge density and overall M-O bond strength [21]. Underlying Ir^{4+} was speculated to be partly oxidized to result in sub-

stoichiometric TiO_{2-x} outer layer, significantly elevating the electrical conductivity. Even for much thicker TiO_2 coating (greater than1 μm) in this study, Ir ions might be diffused into the TiO_2 matrix during the thermal annealing, leading to a vertical concentration gradient of Ir (in mixture with Ti). Effective ionic radius of Ir^{4+} (62.5 pm) is more similar with Ti^{4+} (60.5 pm) than Bi^{3+} (103 pm), supporting the observed enhancement only with the TiO_2–L layer. For the TiO_2–H heterojunction anode, more pronounced increase in ohmic resistance led to net reduction in anodic wave, as in the case of far thicker (~30 μm) TiO_2 layers on $IrTaO_y$ in our previous report [11].

3.3. Reactive chlorine generation by $IrTaO_y/(Bi_2O_3)_x(TiO_2)_{1-x}$ heterojunction anodes

Reactive chlorine generation was comparatively evaluated in 50 mM NaCl solutions (Fig. 3) at variable applied anodic potentials (2.0, 2.5, and 3.0 V NHE). Throughout this study, the corresponding cell voltage and ohmic resistance (measured by current interruption at 200 mA) ranged 4–6 V and 3.3–5.6 Ω, respectively. The current density in potentiostatic condition (Fig. 3a) was in general agreement with the LSV shown in Fig. 2b. EE always decreased with the greater applied potential (cell voltage) due to the increment in ohmic drop, whereas CE varied insignificantly. Despite moderate variations in ohmic drop and iR-compensated anodic potential among anodes, the insignificant dependency of CE on the applied potential would allow a qualitative comparison. The CE and EE values of the control $IrTaO_y$ electrode were averaged to 52% and 4.23 mmol Wh^{-1} at 2.5 V NHE, respectively, while the heterojunction layers substantially augmented the CE and EE for RCS generation (in Fig. 3b and d). Accordingly, despite the general reductions in the operational current density, heterojunction anodes marked greater specific RCS generation rates (Fig. 3c) than the control. The most remarkable enhancement was noted for TiO_2-L with more than 70% increase in SR_{RCS}, due to the elevated voltammetric response. Utilizing nanoparticle slurry precursor with relatively simple preparation procedure, these results outperformed our previous report on $IrTaO_y/Bi_xTi_{1-x}O_z$ heterojunction anodes by casting aqueous Ti-glycolate solutions prepared by a peroxo-route [11].

It would be a rational postulation that the RCS generation through charge transfer between the physi-sorbed ·OH and Cl^- (Eq. (5)) would be far more facile than oxygen atom transfer from higher oxide (Eq. (6)) [5]. In comparison, the $>MO_{x+1}$ form would more preferentially mediate OER (Eq. (4)) than ($>MO_x$ (·OH), Eq. (3)) [10]. Therefore, the speciation of hydrous metal oxide under an anodic bias (MO_x(·OH) versus MO_{x+1}) is expected to determine the selectivity between OER and ClER [22], [23]. More predominant steady-state surface concentration of $>MO_x$(·OH) would account for the overall enhancements of CE and EE for RCS generation on heterojunction architectures, as suggested previously [11], [13]. In order words, primary Ti^{4+} species on surface of heterojunction anodes would prevent transformation into the higher oxide, whereas the control $IrTaO_y$ would favor $>MO_{x+1}$ formation by Ir^{4+}/Ir^{6+} transition.

Compared to $IrTaO_y/TiO_2$ anodes, on the other hand, Bi_2O_3 particles on surface generally lessened the CE_{RCS} and EE_{RCS}, except for $(Bi_2O_3)_3(TiO_2)_7$-H. Our previous report [11] proposed competitive roles of Bi mixing for ClER on the solution casted $IrTaO_y/Bi_xTi_{1-x}O_z$ heterojunction anodes; accelerating interaction with Cl^- (*via* a positive shift in surface charge) but hampering ClER kinetics through the higher oxide formation (*via* Bi^{3+}/Bi^{5+} redox transition). Accordingly, CE values of ClER were noted to be maximized at Bi fraction of 0.1–0.3 [11]. In this study, the former effect was insignificant, most presumably because of spatially separated TiO_2 and Bi_2O_3 phase. Nevertheless, $(Bi_2O_3)_3(TiO_2)_7$-H with the highest surface loading of Bi showed comparable CE and EE values with $IrTaO_y/TiO_2$ anodes.

Although the improved CE and EE of RCS generation on $(Bi_2O_3)_3(TiO_2)_7$-H, limited stability in anodic environments was noted specifically due to the dissolution of Bi_2O_3 particles. Figure S6a illustrates the concentrations of Bi and Ti in electrolyte during an accelerated life test at 1000 mA cm^{-2} operation for the $(Bi_2O_3)_3(TiO_2)_7$-H heterojunction anode. Bi_2O_3 particles were expected to maintain intrinsic properties so as to be vulnerable to anodic potential bias and local acidity from OER, as confirmed by a distinct accumulation of Bi in electrolyte. EDS mapping (Figure S6b-f) after the life test also located intensified signals of Ir on remains with dissolution/detachment of Bi_2O_3 particles. The concurrent rise of Ti concentration would be associated with detachment of TiO_2 nanoparticles along with the collapse of particle aggregation. In summary, decoration of micron-sized Bi_2O_3 particles on the TiO_2 heterojunction brought about limited or even adverse effects both for RCS generation and stability.

3.4. Reactive chlorine generation by $IrTaO_y/Bi_3Ti_7O_x$ heterojunction anodes

In order to address the drawbacks of Bi_2O_3 decoration, this study evaluated two different $Bi_3Ti_7O_x$ heterojunction layers with more uniform doping of Bi into the TiO_2 matrix. For $Bi_3Ti_7O_x$-1 anode, titanium glycolate nano-particle slurry was prepared by polyol-mediated synthesis [14], to be mixed with a bismuth citrate solution (Bi:Ti = 3:7) overnight. During this process, Bi^{3+} was expected to be randomly substituted with Ti^{4+} in the polyol structure by ligand exchange to form a homogeneous solid mixture during the subsequent thermal decomposition. In addition, a well-established co-precipitation procedure for metal ion doped nano-sized TiO_2 colloidal suspension [24] was employed for preparation of $Bi_3Ti_7O_x$-2 anode. Under the same spraying procedure, the mass loading of $Bi_3Ti_7O_x$-1 layer was far greater (3.20 mg cm^{-2}) than $Bi_3Ti_7O_x$-2 (0.342 mg cm^{-2}) due to the different precursor viscosity (aqueous versus organic solvent).

The SEM images on the horizontal surface of $Bi_3Ti_7O_x$ anodes (Figure S7) showed rugged morphology without specific grains of Bi_2O_3. The outer film contained multiple cracks that have been typically found for annealed mixed metal oxide due to the variable thermal expansion coefficients [25]. In addition, XRD profiles (Fig. 4 and S8) for the both $Bi_3Ti_7O_x$ anodes showed insignificant peaks relevant to Bi_2O_3. These observations would substantiate homogeneous mixed metal oxide formation by the modified preparation schemes. Besides reflections from Ti substrate, intense signals from rutile TiO_2 dominated on $Bi_3Ti_7O_x$-2. Insertion of Bi^{3+} into the TiO_2 lattice would distort the crystalline structure to facilitate transformation of anatase to rutile at relatively low annealing temperature (450 °C) [16]. At superimposable locations, by far smaller peaks were noted on $Bi_3Ti_7O_x$-1, suggesting predominant amorphous phase. Evidences were presented that polyol-mediated Ti-glycolate could remain amorphous up to 500 °C [14].

CV presented in Figure S9a estimated areal capacitance to be 14.91 mF cm^{-2} and 21.96 mF cm^{-2} for $Bi_3Ti_7O_x$-1 and −2, respectively. Moderately lower capacitance of $Bi_3Ti_7O_x$-1 would be associated with the greater mass loading of outer layer and film resistance. During the LSV in 50 mM NaCl solutions (Figure S9b), anodic current waves on $Bi_3Ti_7O_x$ anodes outperformed $(Bi_2O_3)_3(TiO_2)_7$–H anodes and the voltammogram of $Bi_3Ti_7O_x$-1 was comparable with TiO_2-H. Despite the lack of conclusive evidence, coordinately unsaturated active sites in amorphous structure ($Bi_3Ti_7O_x$-1) could moderately facilitate the kinetics of OER and ClER. Fig. 5 shows that both $Bi_3Ti_7O_x$ anodes marked CE_{RCS} near unity (93.6% and 98.3%, on average). Consequently, the $IrTaO_y/Bi_3Ti_7O_x$ heterojunction anodes marked the highest EE_{RCS} (8.02–8.16 mmol Wh^{-1} at 2.5 V NHE) among the anodes interrogated in this study. These electrodes even outperformed a commercial Ir based DSA (De Nora) which showed lower values of CE_{RCS} (40.9% on average) and EE_{RCS} (3.1 mmol Wh^{-1} at 2.5 V NHE) as shown in Figure S10. These results demonstrated

that even with the analogous composition, mixing level of constituents could significantly affect the electronic and electrostatic properties. In particular, relatively homogenous intercalation of Bi component might avoid the ohmic resistance across multiple junctions, while increase the point of zero charge for enhanced electro-sorption of Cl^-. Furthermore, accelerated life test at 1000 mA cm^{-2} indicated insignificant dissolution of Bi and Ti during operation for 30 h (data not shown).

In order to evaluate the effects of ion migration upon the potential bias (increasing [Cl^-] in the anode vicinity), the RCS generation experiments were performed in 50 mM NaCl solutions with or without another electrolyte (50 mM $NaClO_4$) under a galvanostatic condition (Figure S11). The measured values of SR_{RCS}, CE_{RCS}, and EE_{RCS} in the mixed solutions were 82, 86, and 97% of those in NaCl solutions, respectively. Moderate reductions could be associated with the competing ion migration and lower potential bias in the presence of other electrolyte, which would be a consideration to understand the performance in real (waste)water matrix. On the other hand, one may argue that the elevated CE_{RCS} by the heterojunction architecture would be ascribed to the reduced current density, since an increasing current could invigorate OER only when ClER is rate-limited by diffusion of Cl^-. However, the operational current density in this study would be lower than the limiting current density for ClER, as corroborated by Figure S12. The observed CE_{RCS} values showed negligible correlation with the current density. Therefore, the shift in ClER selectivity should be understood by speciation of surface intermediates with variable reactivity with Cl^- (*vide infra*).

3.5. Formate ion degradation versus RCS generation to assess intermediate speciation

In this study, the hydroxyl radical (·OH) on anode surface could be a nonselective oxidant to be utilized for Cl^- oxidation to RCS. Due to the short lifetime (10^{-6} – 10^{-3} s), free or bound ·OH has been quantified using an array of probe compounds such as salicylic acid, benzoic acid, coumarin, benzoquinone, and RNO (*p*-nitrosodimethylaniline) [26]. Formate ion could be another surface ·OH prove due to superb reactivity with ·OH [27], simple quantification method using IC, and relatively low molecular weight to avoid diffusion limitation.

In order to further interrogate the speciation between MO_x(·OH) and MO_{x+1} and their roles on RCS generation, potentiostatic (E_a = 2.0 or 2.5 V NHE) formate ion degradation experiments (initial concentration = 50 mM) were performed using the series of $(Bi_2O_3)_x(TiO_2)_{1-x}$ and $Bi_3Ti_7O_x$ heterojunction anodes (Figure S13). We limited the applied anodic potential up to 2.5 V NHE due to slightly lower electrical conductivity of 50 mM NaCOOH solutions (4.3 mS cm^{-1}) than 50 mM NaCl solutions (5.4 mS cm^{-1}). The differences in ohmic drop between two solutions were estimated to be 0.16 V at maximum. The reaction between $HCOO^-$ and > MO_x(·OH) could be approximated to pseudo-first-order owing to the facile kinetics (Eq. (10)).

$$>MO_x(\cdot OH) + HCOO^- \rightarrow >MO_x + COO^{-}\cdot + H_2O \quad (10)$$

Fig. 6a illustrates the observed pseudo-first-order rate constants of formate decay ($k_{obs}^{formate}$) in relation with the pseudo-first order rate constants of RCS generation (k_{obs}^{ClER}) that were estimated from the SR_{RCS} (Figs. 3c and 5c) and initial chloride concentration ($k_{obs}^{ClER} = SR_{RCS}\, A\, /V\, [Cl^-]_0$). The k_{obs}^{ClER} was observed to be linearly correlated with $k_{obs}^{formate}$ and, more importantly, the slope of the regressed line was close to the ratio of bimolecular rate constant of ·OH with Cl^- ($k_{\cdot OH}^{chloride} = 4.3 \times 10^9$ M^{-1} s^{-1}) to that

with $HCOO^-$ ($k_{\cdot OH}^{formate} = 3.2 \times 10^9\ M^{-1}\ s^{-1}$). These findings strongly evinced that $MO_x(\cdot OH)$ would be the exclusive intermediate for the RCS generation (Eq. (5)), while MO_{x+1} driven ClER (Eq. (6)) would play a minor role for our heterojunction anodes. In spite of previous reports [28] on HCOOH degradation by IrO_2/IrO_3 couple in acid (pH 0), oxygen atom transfer from MO_{x+1} to $HCOO^-$ could be excluded in the current experimental conditions. Ozone, as a presumed analog of the higher oxide, is known to undergo sluggish kinetics both with Cl^- ($<3 \times 10^{-3}\ M^{-1}\ s^{-1}$) and $HCOO^-$ ($1 \times 10^2\ M^{-1}\ s^{-1}$) [29], [30].

Provided that free and bound ·OH react with $HCOO^-$ at analogous bimolecular rate constants, the steady-state concentration of surface bound ·OH ($[>MO_x(\cdot OH)]_{SS}$) could be estimated from $k^{obs}_{formate}$ using eq. (11).

$$[>MO_x(\cdot OH)]_{SS} = k_{obs}^{formate}\ (s^{-1})\ V / (A\ k_{\cdot OH}^{formate}) \quad (11)$$

As shown in Figure S14a, the $[>MO_x(\cdot OH)]_{SS}$ estimates were in similar order with our previous study [11]. Eq. (12) given by a pseudo-steady-state approximation further estimated the rate constant for Eq. (2) (k_2), assuming that $>MO_x(\cdot OH)$ and $>MO_{x+1}$ are exclusively responsible to the formate ion oxidation and OER, respectively.

$$k_2 = \frac{CE_{OER}\ I}{2F} \times \frac{1}{A[> MO_x\ (\quad OH)]_{SS}} \quad (12)$$

where CE_{OER} is the CE of OER calculated from the charge balance (1 – CE of formate ion degradation). Figure S14b substantiated that the outer heterojunction layers significantly lowered k_2 values of $IrTaO_y$. Under further assumption that transition from $>MO_x(\cdot OH)$ to $>MO_{x+1}$ (Eq. (2)) is limiting the OER rate, CE_{RCS} would be determined by the ratio of k_2 to $k_{obs}^{chloride}$. Despite the apparent inverse relation between k_2 and CE_{RCS} noted in Fig. 6b, relatively weak correlation suggested the liberation of O_2 from $>MO_{x+1}$ (Eq. (4)) could also determine the OER rate depending on the outer layer composition. For example, a strong binding of O on Bi might allow the ClER to overwhelm OER on the $Bi_3Ti_7O_x$-2 anode with relatively high k_2 value.

4. Conclusions

This study prepared $Ir_7Ta_3O_y$ DSAs with outer heterojunction layers based on mixed Bi and Ti oxide to compare the RCS generation efficiency during competitive OER and ClER in dilute (50 mM) NaCl solutions. Crack free, anatase dominant TiO_2 layers prepared from ball-milled P60 nanoparticles brought about significantly enhanced SR_{RCS}, CE_{RCS}, and EE_{RCS}, while TiO_2-L even elevated the anodic current wave possibly owing to a tuned overall M-O bond strength. However, decoration of Bi_2O_3 particles on the outer TiO_2 films ($(Bi_2O_3)_x(TiO_2)_{1-x}$) gave limited or adverse effects on voltammetric response, RCS generation, and stability presumably because of multiple junction formation and specially separated Bi_2O_3 phase. To this end, $Bi_3Ti_7O_x$ heterojunction layers with elevated mixing level of Bi marked CE_{RCS} values near unity, by an effective increase in the point of zero charge. Consequently, the highest SR_{RCS} and EE_{RCS} were noted by $Ir_7Ta_3O_y/TiO_2$-L and $Ir_7Ta_3O_y/Bi_3Ti_7O_x$, respectively. Parallel formate ion degradation experiments revealed that the RCS generation would be exclusively mediated by >MO (·OH)

x

whose further transition to $>MO_{x+1}$ was proven to be retarded by the heterojunction layer. Our heterojunction anodes with simplified preparation procedure would allow an energy-efficient electrochemical oxidation processes for water disinfection and high salinity wastewater treatment through the enhanced chlorine evolution. Improvements in the industrial chlorine generation (chlor-alkali process) are also expected with reduced power input and operational cost. Further study should tackle the effects of outer layer TiO_2 loading (thickness) on film resistance and CE_{RCS}, as well as stability of the Bi-doped TiO_2 layers in more systematic manners based on periodic CE_{RCS} measurements during accelerated life test.

Acknowledgment

The authors would like to acknowledge the financial support of the Bill and Melinda Gates Foundation (BMGF RTTC Grant OPP1149755). This work was also supported by the Basic Research Laboratory (NRF-2018R1A4A1022194), Young Researcher Program (NRF-2019R1C1C1003435), and Nano Material Technology Development Program (NRF-2016M3A7B4908161) through the National Research Foundation of Korea.

Footnotes

Appendix A Supplementary data to this article can be found online at https://doi.org/10.1016/j.jcat.2020.04.009.

Appendix A. Supplementary material

The following are the Supplementary data to this article:

Supplementary data 1:

References

1. Hu W., Wang Y., Hu X., Zhou Y., Chen S. Three-dimensional ordered macroporous IrO2 as electrocatalyst for oxygen evolution reaction in acidic medium. J. Mater. Chem. 2012;22

2. Mamaca N., Mayousse E., Arrii-Clacens S., Napporn T.W., Servat K., Guillet N., Kokoh K.B. Electrochemical activity of ruthenium and iridium based catalysts for oxygen evolution reaction. Appl. Catal. B. 2012;111–112:376–380.

3. Menzel N., Ortel E., Mette K., Kraehnert R., Strasser P. Dimensionally Stable Ru/Ir/TiO2-Anodes with Tailored Mesoporosity for Efficient Electrochemical Chlorine Evolution. ACS Catal. 2013;3:1324–1333.

4. Comninellis C., Vercesi G.P. Characterization of DSA®-Type Oxygen Evolving Electrodes: Choice of a Coating. 1991;21:335–345.

5. Chung C.M., Lee W., Hong S.W., Cho K. Effects of anode materials and chloride ions on current efficiency of electrochemical oxidation of carbohydrate compounds. J Electrochem Soc. 2019;166:H628–H634.

6. Hansen H.A., Man I.C., Studt F., Abild-Pedersen F., Bligaard T., Rossmeisl J. Electrochemical chlorine evolution at rutile oxide (110) surfaces. Phys Chem Chem Phys. 2010;12:283–290. [PubMed: 20024470]

7. M. Panizza, G.J.C.r. Cerisola, Direct and mediated anodic oxidation of organic pollutants, 109 (2009) 6541–6569. [PubMed: 19658401]

8. Martinez-Huitle C.A., Ferro S. Electrochemical oxidation of organic pollutants for the wastewater treatment: direct and indirect processes. Chem. Soc. Rev. 2006;35:1324–1340. [PubMed: 17225891]

9. Zhang J.-J., Hu J.-M., Zhang J.-Q., Cao C.-N. IrO2–SiO2 binary oxide films: Geometric or kinetic interpretation of the improved electrocatalytic activity for the oxygen evolution reaction. Int. J. Hydrogen Energy. 2011;36:5218–5226.

10. C.J.E.A. Comninellis, Electrocatalysis in the electrochemical conversion/combustion of organic pollutants for waste water treatment, 39 (1994) 1857–1862.

11. K. Cho, M.R. Hoffmann, BixTi1–xOz Functionalized heterojunction anode with an enhanced reactive chlorine generation efficiency in dilute aqueous solutions, Chemistry of Materials, 27 (2015) 2224–2233.

12. Kronawitter C.X., Vayssieres L., Shen S., Guo L., Wheeler D.A., Zhang J.Z., Antoun B.R., Mao S.S. A perspective on solar-driven water splitting with all-oxide hetero-nanostructures. Energy Environ. Sci. 2011;4

13. Exner K.S., Anton J., Jacob T., Over H. Controlling Selectivity in the Chlorine Evolution Reaction over RuO2-Based catalysts. Angew. Chem. Int. Ed. 2014;53:11032–11035. [PubMed: 25154724]

14. Wei Y., Zhu J.X., Gan Y.X., Cheng G. Titanium glycolate-derived TiO2 nanomaterials: Synthesis and applications. Adv Powder Technol. 2018;29:2289–2311.

15. Kraft A., Stadelmann M., Blaschke M., Kreysig D., Sandt B., Schröder F., Rennau J. Electrochemical water disinfection Part I: Hypochlorite production from very dilute chloride solutions. Journal of Applied Electrochemistry. 1999;29:859–866.

16. Hanaor D.A.H., Sorrell C.C. Review of the anatase to rutile phase transformation. J. Mater. Sci. 2010;46:855–874.

17. Ardizzone S., Bianchi C.L., Cappelletti G., Ionita M., Minguzzi A., Rondinini S., Vertova A. Composite ternary SnO2–IrO2–Ta2O5 oxide electrocatalysts. J. Electroanal. Chem. 2006;589:160–166.

18. Liu X., You B., Yu X.-Y., Chipman J., Sun Y. Electrochemical oxidation to construct a nickel sulfide/oxide heterostructure with improvement of capacitance. J. Mater. Chem. A. 2016;4:11611–11615.

19. Hou Y.-Y., Hu J.-M., Liu L., Zhang J.-Q., Cao C.-N. Effect of calcination temperature on electrocatalytic activities of Ti/IrO2 electrodes in methanol aqueous solutions. Electrochim. Acta. 2006;51:6258–6267.

20. Cooper K.R., Smith M. Electrical test methods for on-line fuel cell ohmic resistance measurement. J. Power Sources. 2006;160:1088–1095.

21. Finke C.E., Omelchenko S.T., Jasper J.T., Lichterman M.F., Read C.G., Lewis N.S., Hoffmann M.R. Enhancing the activity of oxygen-evolution and chlorine-evolution electrocatalysts by atomic layer deposition of TiO2. Energy Environ. Sci. 2019;12:358–365.

22. Rossmeisl J., Qu Z.W., Zhu H., Kroes G.J., Nørskov J.K. Electrolysis of water on oxide surfaces. J. Electroanal. Chem. 2007;607:83–89.

23. S.J.E.A. Trasatti, Electrocatalysis in the anodic evolution of oxygen and chlorine, 29 (1984) 1503–1512.

24. W.Y. Choi, A. Termin, M.R. Hoffmann, The Role of Metal-Ion Dopants in Quantum-Sized Tio2 - Correlation between Photoreactivity and Charge-Carrier Recombination Dynamics, J Phys Chem-Us, 98 (1994) 13669–13679.

25. L. Da Silva, V. Alves, M. Da Silva, S. Trasatti, J.J.E.A. Boodts, Oxygen evolution in acid solution on IrO2+ TiO2 ceramic films. A study by impedance, voltammetry and SEM, 42 (1997) 271-281.

26. Nosaka Y., Nosaka A.Y. Generation and detection of reactive oxygen species in photocatalysis. Chem. Rev. 2017;117:11302–11336. [PubMed: 28777548]

27. Kesselman J.M., Weres O., Lewis N.S., Hoffmann M.R. Electrochemical production of hydroxyl radical at polycrystalline Nb-doped TiO2 electrodes and estimation of the partitioning between hydroxyl radical and direct hole oxidation pathways. J. Phys. Chem. B. 1997;101:2637–2643.

28. Fierroa S., Ouattara L., Calderon E.H., Passas-Lagos E., Baltruschat H., Comninellis C. Investigation of formic acid oxidation on Ti/IrO2 electrodes. Electrochim. Acta. 2009;54:2053–2061.

29. Neta P., Huie R.E., Ross A.B. Rate constants for reactions of inorganic radicals in aqueous solution. J. Phys. Chem. Ref. Data. 1988;17:1027–1284.

30. Buxton G.V., Greenstock C.L., Helman W.P., Ross A.B. Critical review of rate constants for reactions of hydrated electrons, hydrogen atoms and hydroxyl radicals (OH/ O− in Aqueous Solution. J. Phys. Chem. Ref. Data. 1988;17:513–886.

Figures and Tables

Fig. 1

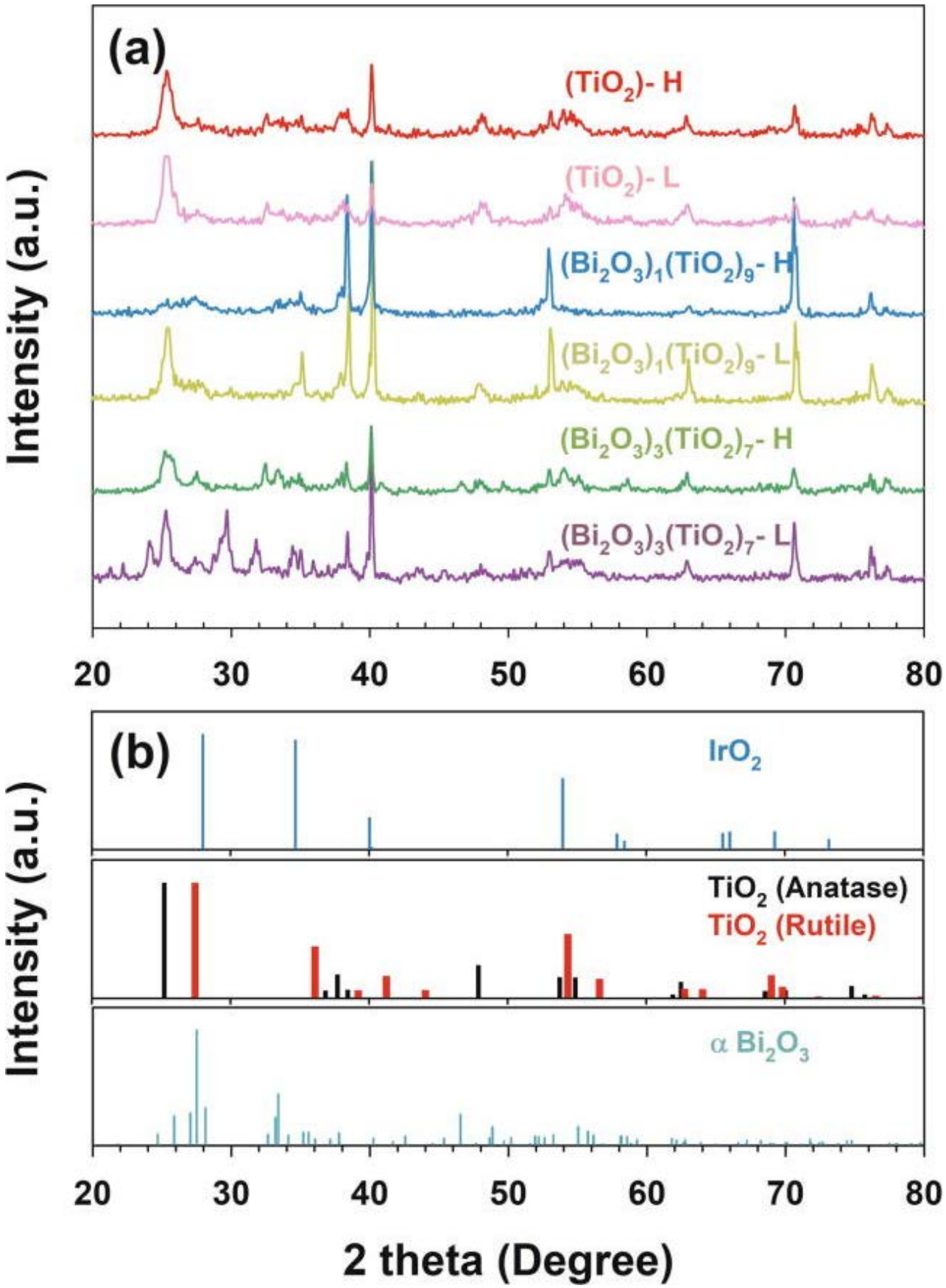

Open in a separate window

(a) X-ray diffraction patterns of (a) $IrTaO_y/(Bi_2O_3)_x(TiO_2)_{1-x}$ heterojunction anodes (x = 0, 0.1, and 0.3, mass

loading = high (H) and low (L)), referenced with (b) IrO_2, TiO_2 (anatase, rutile) and Bi_2O_3.

Fig. 2

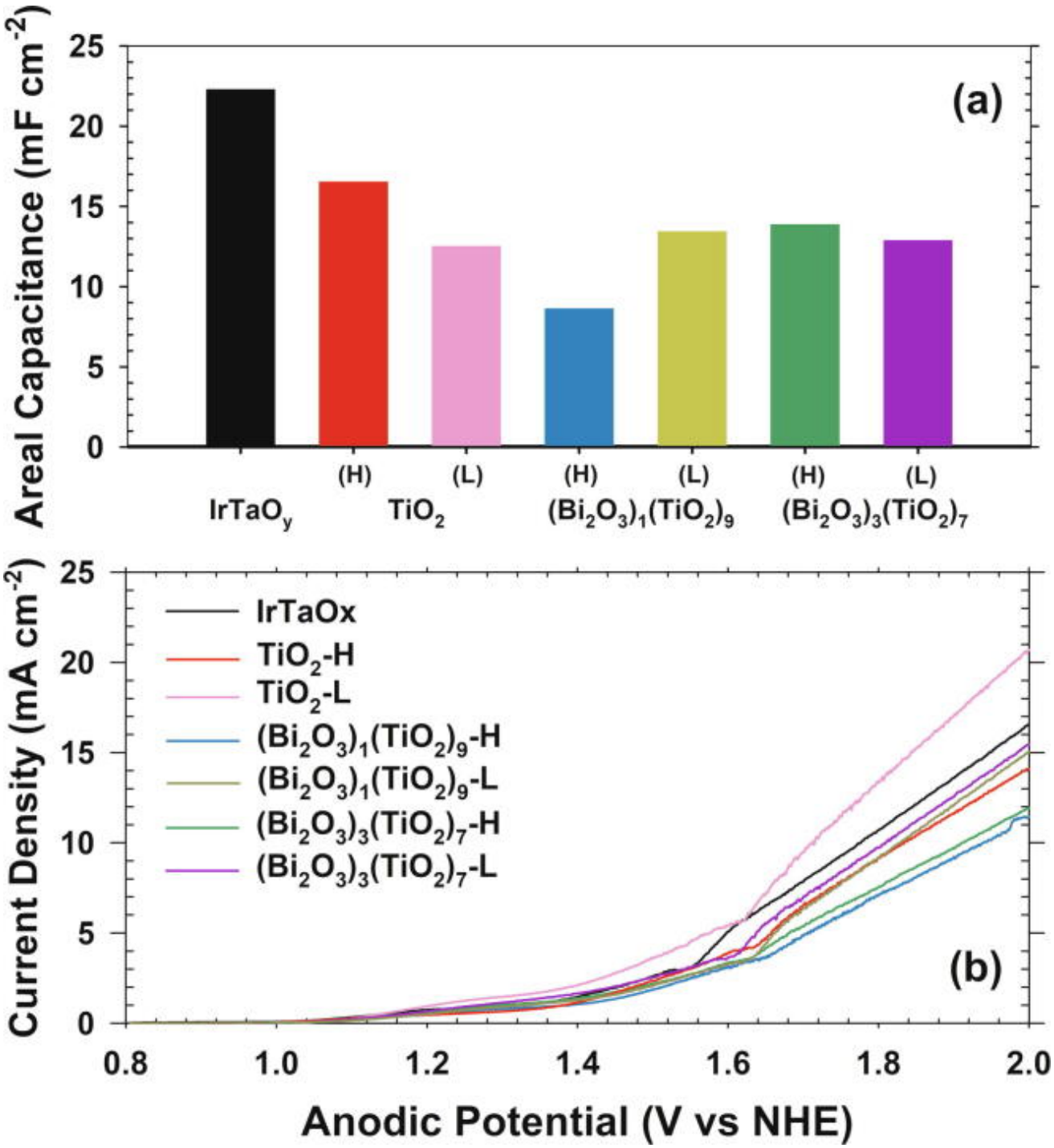

Open in a separate window

(a) Areal capacitance measured by cyclic voltammetry (scan range: 0.2–1.0 V NHE, scan rate: 20 mV s^{-1}) and (b) linear sweep voltammograms (scan range: 0.8–2.0 V NHE, scan rate: 5 mV s^{-1}) of $Ir_7Ta_3O_y/(Bi_2O_3)_x(TiO_2)_{1-x}$ heterojunction anodes (x = 0, 0.1, and 0.3, mass loading = high (H) and low (L)); electrolyte: 50 mM NaCl (pH 7), cathode: stainless steel, geometric surface area: 3 × 2 cm^2. Data for $Ir_7Ta_3O_y$ anode are shown as references.

Table 1

Anodic potential at 10 mA cm^{-2} in linear sweep voltammetry (scan range: 0.8–2.0 V NHE, scan rate: 5 mV s^{-1}) and solution resistance (R_S) measured by current interruption (200 mA); electrolyte: 50 mM NaCl (pH 7), cathode: stainless steel, geometric surface area: 3 × 2 cm^2.

Electrode	E_a (V, j = 10 mA cm^{-2})	R_S from current interruption (Ω)
$IrTaO_x$	1.777	4.115
TiO_2-H	1.834	4.090
TiO_2-L	1.716	3.414
$(Bi_2O_3)_1(TiO_2)_9$-H	1.940	4.846
$(Bi_2O_3)_1(TiO_2)_9$-L	1.829	3.676
$(Bi_2O_3)_3(TiO_2)_7$-H	1.912	5.427
$(Bi_2O_3)_3(TiO_2)_7$-L	1.809	4.054
$Bi_3Ti_7O_x$-1	1.862	4.455
$Bi_3Ti_7O_x$-2	1.887	5.383

Fig. 3

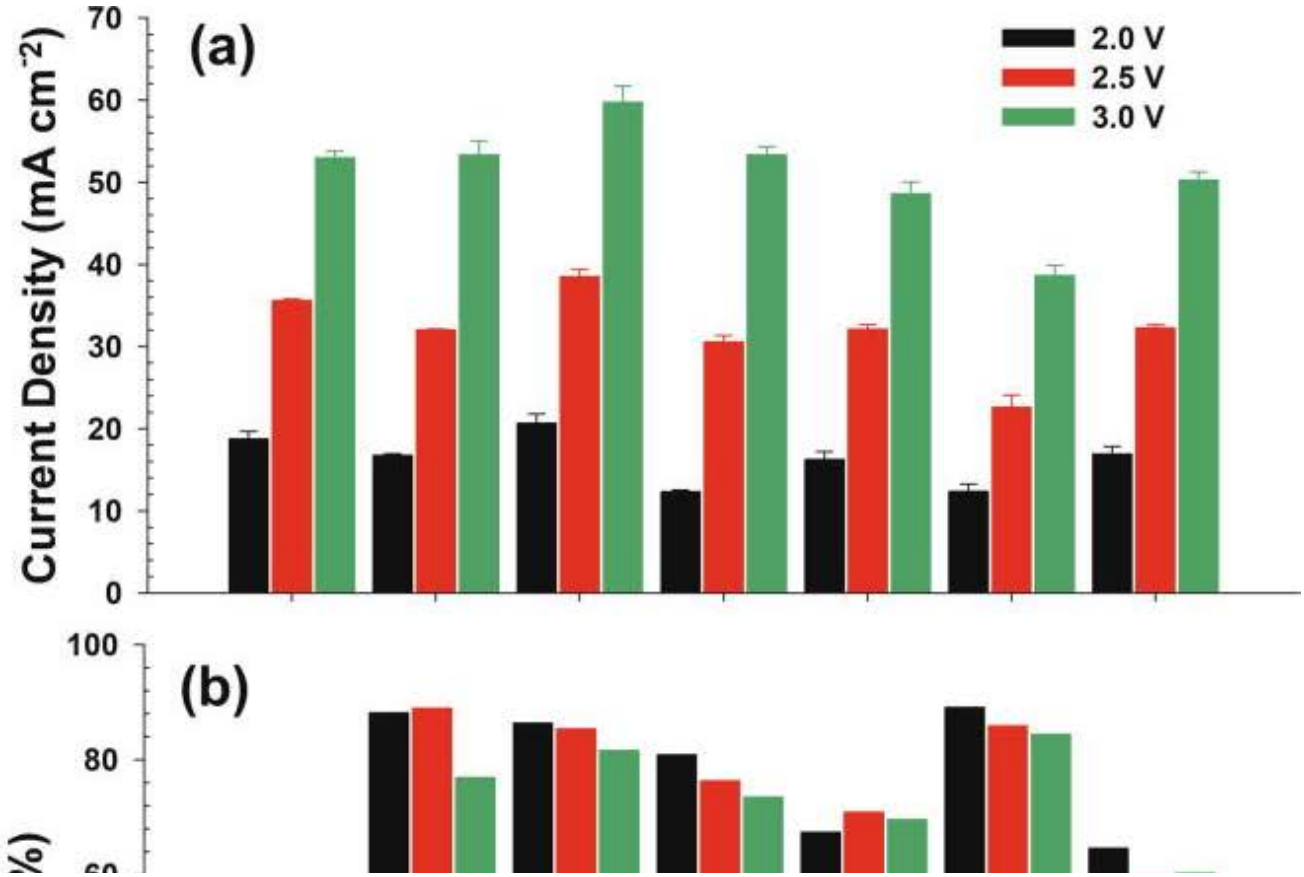

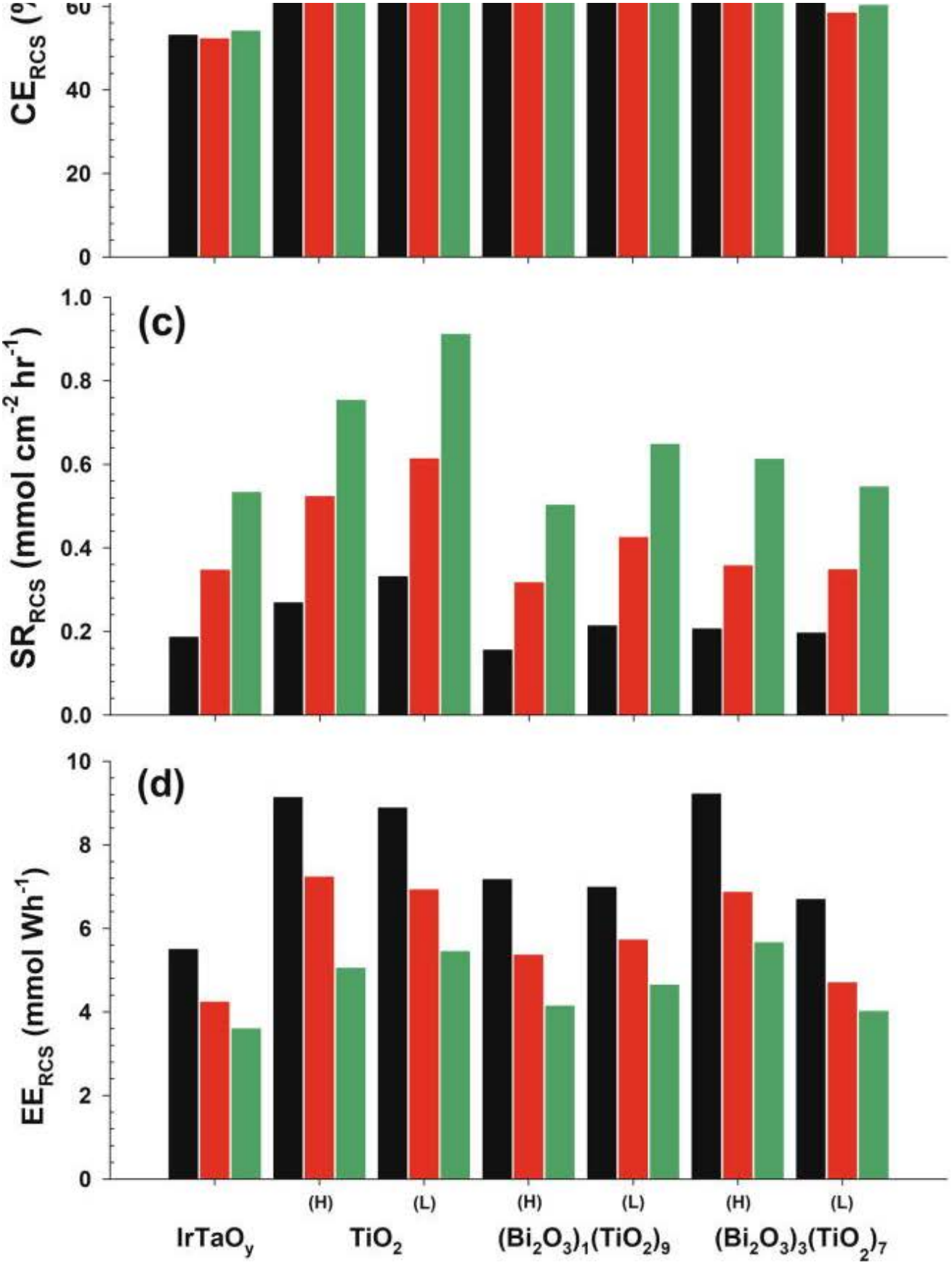

Open in a separate window

(a) Current density, (b) current efficiency, (c) specific rate and (d) energy efficiency of reactive chlorine species generation during potentiostatic electrolysis of 50 mM NaCl solutions (pH 7) with $IrTaO_y/(Bi_2O_3)_x(TiO_2)_{1-x}$ heterojunction anodes

(x = 0, 0.1, and 0.3; mass loading = high (H) and low (L)); cathode: stainless steel, geometric surface area: 3 × 2 cm^2, applied anodic potential: 2.0, 2.5, and 3.0 V NHE. Data for $IrTaO_y$ anode are shown as references.

Fig. 4

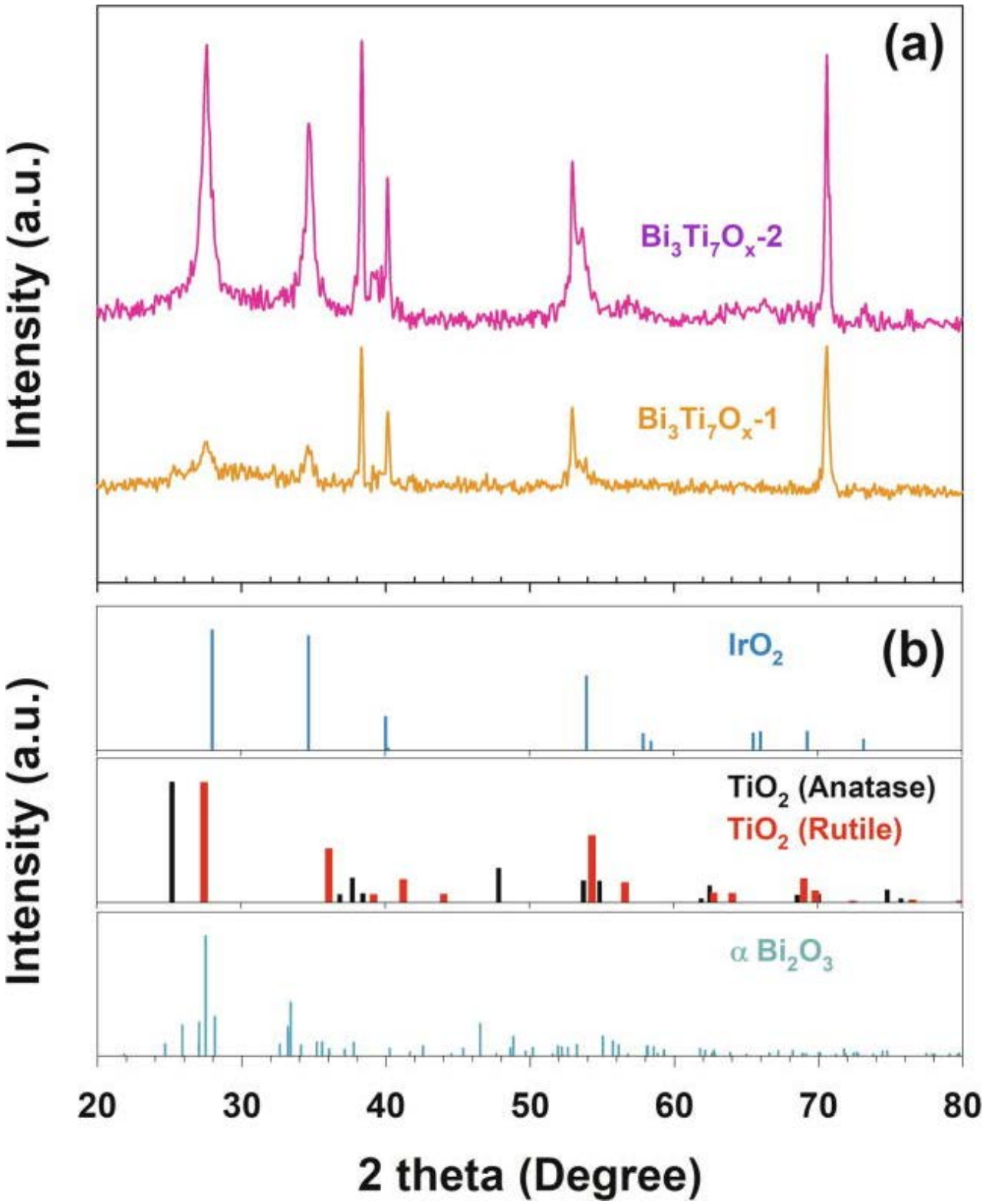

Open in a separate window

(a) X-ray diffraction patterns of (a) $IrTaO_y/(Bi_3Ti_7O_x$-1, 2) heterojunction anodes, referenced with (b) IrO_2, TiO_2 (anatase, rutile) and α-Bi_2O_3.

Fig. 5

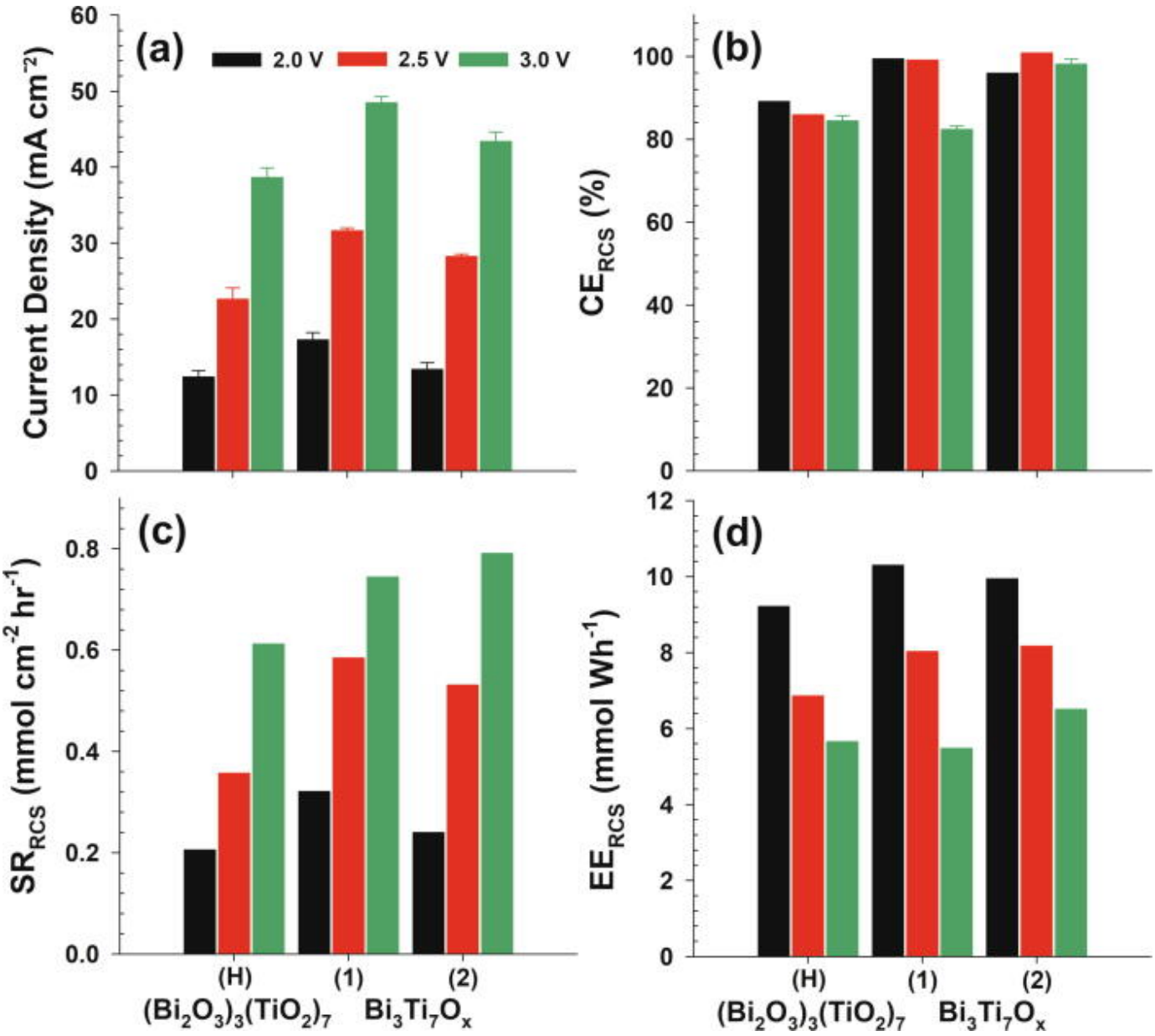

(a) Current density, (b) current efficiency, (c) specific rate and (d) energy efficiency of reactive chlorine species generation during potentiostatic electrolysis of 50 mM NaCl solutions (pH 7) with $IrTaO_y/(Bi_3Ti_7O_x$-1, 2) heterojunction anodes; cathode: stainless steel, geometric surface area: 3 × 2 cm^2, applied anodic potential: 2.0, 2.5, and 3.0 V NHE. Data for $IrTaO_y/(Bi_2O_3)_3(TiO_2)_7$-H anode are shown as references.

Fig. 6

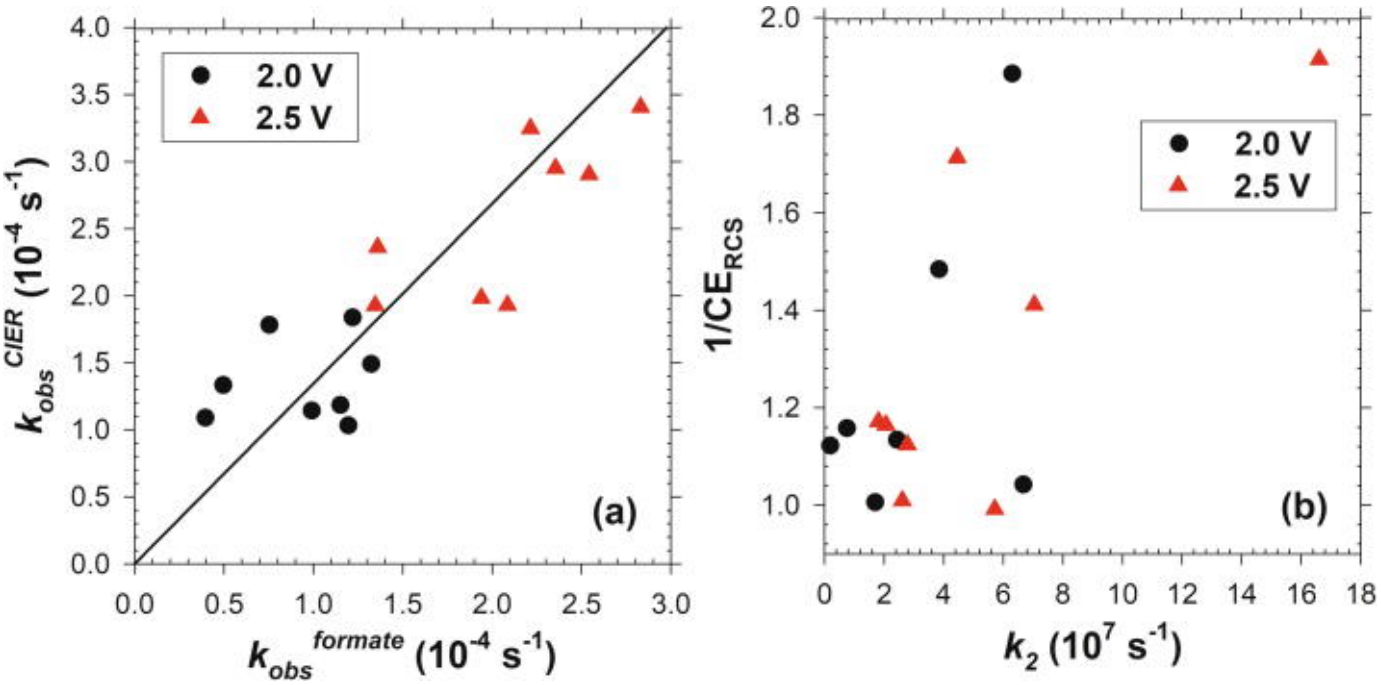

Correlations between (a) rate constants of ClER (k_{obs}^{ClER}) and formate degradation ($k_{obs}^{formate}$), together with (b) current efficiency of reactive chlorine generation (CE_{RCS}) and transition rate constant (k_2) from $MO_x(\cdot OH)$ to MO_{x+1}.